AGU PUBLICATIONS

JGR

Journal of Geophysical Research: Space Physics

RESEARCH ARTICLE

10.1002/2013JA019476

Key Points:
- Plumes interact with LEO plasma/B-field
- Thruster burns associated with enhanced plasma flux
- Simulation model reproduces in situ observation data

Correspondence to:
K. A. Stephani,
ksteph@illinois.edu

Citation:
Stephani, K. A., I. D. Boyd, R. L. Balthazor, M. G. McHarg, B. A. Mueller, and R. J. Adams (2014), Analysis and observation of spacecraft plume/ionosphere interactions during maneuvers of the space shuttle, *J. Geophys. Res. Space Physics*, *119*, 7636–7648, doi:10.1002/2013JA019476.

Received 24 SEP 2013
Accepted 8 AUG 2014
Accepted article online 11 AUG 2014
Published online 2 SEP 2014

Analysis and observation of spacecraft plume/ionosphere interactions during maneuvers of the space shuttle

K. A. Stephani[1], I. D. Boyd[1], R. L. Balthazor[2], M. G. McHarg[2], B. A. Mueller[2], and R. J. Adams[3]

[1]Department of Aerospace Engineering, University of Michigan, Ann Arbor, Michigan, USA, [2]USAF Academy, Fairchild Drive, Colorado, USA, [3]Barron Associates, Inc., Charlottesville, Virginia, USA

Abstract This work employs in situ measurement data and constructive simulations to examine the underlying physical mechanisms that drive spacecraft plume interactions with the space environment in low-Earth orbit. The study centers on observations of the enhanced flux of plasma generated during a maneuver of Space Shuttle Endeavour as part of the Sensor Test for Orion Relative Navigation Risk Mitigation experiment in May 2011. The Canary electrostatic analyzer (ESA) instrument mounted on the portside truss of the International Space Station indicated an elevated ion current during the shuttle maneuver. The apparent source of enhanced ion current is a result of interaction of the spacecraft thruster plume with the rarefied ambient ionosphere, which generates regions of relatively high density plasma through charge exchange between the neutral plume and ambient ions. To reconstruct this event, unsteady simulation data were generated using a combined direct simulation Monte Carlo/particle-in-cell methodology, which employed detailed charge exchange cross-section data and a magnetic field model. The simulation provides local plasma characteristics at the ESA sensor location, and a sensor model is subsequently used to transform the local properties into a prediction of measured ion current. The predicted and observed total currents are presented as a function of time over a 30 s period of pulsed thruster firings. A strong correlation is observed in the temporal characteristics of the simulated and measured total current, and good agreement is also achieved in the total current predicted by the model. These results support conclusions that (1) the enhanced flux of plasma observed by the ESA instrument is associated with Space Shuttle thruster firings and (2) the simulation model captures the essential features of the plume interactions based on the observation data.

1. Introduction

Spacecraft thruster firings occur often in low-Earth orbit (LEO) as a means of altering the trajectory of a space vehicle. A fundamental understanding of plume dynamics in this rarefied plasma environment is imperative for developing both predictive and mitigatory capabilities to avoid plume impingement on critical spacecraft surfaces. Chemical interactions between post combustion neutral species generated by spacecraft thrusters and ambient ions in the upper atmosphere play an important role in determining the dynamic behavior of these plumes. In particular, the high-density neutral plume emitted during a thruster burn is subject to charge exchange reactions with the ambient ions. This interaction can alter the local ionospheric properties and lead to excitation of plasma waves. Studies of such interactions, both experimental and computational, have been centralized around LEO transportation spacecraft, including Space Shuttle, Soyuz, Progress, and the Mir space station [e.g., *Burke et al.*, 1995; *McMahon et al.*, 1983; *Karabadzhak et al.*, 1997; *Drakes and Swann*, 1999; *Kaplan and Bernhardt*, 2010; *Bernhardt et al.*, 2012].

The study by *Burke et al.* [1995] examined the energy distribution of positive, single-charge ions detected by the Shuttle Potential and Return Electron Experiment (SPREE) during a thruster burn of the Tethered Satellite System (TSS 1) mission. Data collected by this sensor included information regarding both energy and angular distributions of ions impacting the sensor, over ion energies ranging from 10 to 100 eV. The study by *Burke et al.* [1995] also compared SPREE data with results from a two-dimensional collisionless molecular model. The model tracked trajectories of neutrals and pickup ions (plume-related ions formed through charge transfer of plume neutrals with ambient ions) during a thruster burn event and provided information regarding the distribution of ions that eventually impact the SPREE sensor. This study allowed for a comparison between the measured and predicted ion energy distributions. Their results also

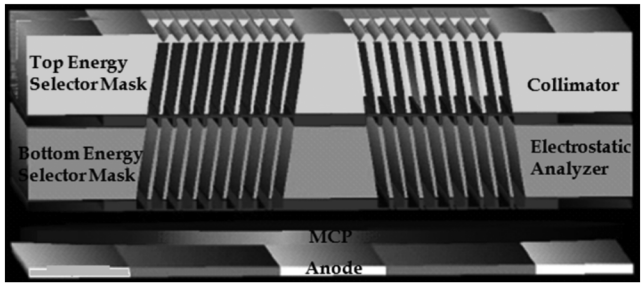

Figure 1. Cross-section schematic of Canary sensor components. Ions enter through collimator at top, then pass through electrostatic analyzer, MCP, and impact the anode at the bottom.

demonstrated that significant scattering occurs near the thruster exit as well as after charge exchange between the neutral gas and ambient oxygen ions.

The present study aims to examine the interaction between Space Shuttle Endeavour's Reaction Control System (RCS) plumes and the ambient ionosphere during the Sensor Test for Orion Relative Navigation Risk Mitigation (STORRM) NH2 maneuver, as observed by the Canary instrument on the International Space Station (ISS). The STORRM rerendezvous maneuver was a fly-around of Space Shuttle Endeavour to the ISS consisting of nine individual maneuvers, including NH2 [*Stuit*, 2011], which is the focus of this study. The NH2 maneuver was a height adjustment maneuver in which five RCS jets (F1U, L2U, L2D, R2U, and R2D) were fired manually by the Endeavour crew over a period of approximately 30 s. Only the F1U, L2U, and R2U jets are considered in this study, as contributions from the L2D and R2D thrusters to the effluent spacecraft plume are negligible. At the time of the NH2 burn sequence, the ISS was located at a longitude of 164° east and a latitude of 51° south. Space Shuttle Endeavour was approaching ISS and was approximately 5 km downstream and 1 km above the ISS orbit. For convenience, we define a coordinate system with its origin fixed to Endeavour's position, an x axis aligned with the vehicle velocity vector, a z axis pointing to nadir, and a y axis completing a right-handed frame. During the NH2 maneuver, the ISS was located 5 km upstream ($+x$ direction) and 1 km below ($+z$ direction) the Space Shuttle. To create a negative change in velocity, Endeavour's RCS jets were firing upstream in the $+x$ direction directly into the ambient ionosphere flow, a condition which will be referred to hereafter as a ram flow configuration [*Stephani and Boyd*, 2014]. Also in this frame of reference, the Earth's geomagnetic field lines were aligned with the z axis, orthogonal to the shuttle velocity vector, and had a velocity equivalent to the orbital velocity relative to the shuttle. The local geomagnetic field lines are assumed to be orthogonal to the trajectory of the ISS at this point (164° longitude east and 51° latitude south), which is a good assumption. At this point on the ISS trajectory, the ISS velocity vector is almost perfectly aligned with lines of constant latitude (east/west), while the Earth's unperturbed geomagnetic field lines are aligned with the longitudinal lines. The NH2 maneuver was short in duration, so it is assumed that the separation distance and relative position of the ISS with respect to the RCS jets remains fixed within these simulations.

In modeling the STORRM NH2 maneuver, this work simulates the interaction of the spacecraft neutral plume with the ambient ionosphere, starting from the plume expansion at the thruster nozzle exit, up to large distances of greater than 20 km, using a particle-based fluid flow model. These results are then used to conduct an analysis of the total current generated by the resulting ion plume. The Canary instrument provides a time-resolved measure of the total current at the surface of the ISS, as well as the time-resolved energy spectra of the incident ion flux. The goal of this paper is to present a comparison of the unsteady total current observed by Canary with the total current predicted from the particle-based simulations. A description of the Canary instrument is outlined first in section 2, and details regarding the computational framework, physical models, and RCS thruster data are discussed in section 3. The results are presented next in section 4 in two parts. First, the development of the unsteady spacecraft plume is examined over four snapshots in time during the early portion of the NH2 burn sequence. The simulation data are then analyzed, and the predicted total current is compared to the Canary observation data over the duration of the STORRM NH2 maneuver. Concluding remarks are presented in section 5.

Figure 2. SIMION [*Dahl and Delmore*, 1987] calculation of ion trajectories through electrostatic analyzer (used for predicting ESA efficiency).

2. Description of Canary Instrument

The final flight of Space Shuttle Endeavour, STS-134 on 16 May 2011,

Table 1. Geometric Parameters and Instrument Factors of Canary Sensors (1–7)

Sensor	A (m^2)	eV	P_f	$\Delta E/E$	f_{MCP}	f_{ESA}
1	1.53×10^{-6}	0–30	10	0.046	1.0×10^5	0.12
2	9.18×10^{-7}	0–30	10	0.046	1.0×10^5	0.12
3	1.53×10^{-6}	0–30	10	0.046	1.0×10^5	0.12
4	$\mathbf{6.53 \times 10^{-6}}$	**0–66**	**22**	**0.125**	$\mathbf{1.0 \times 10^5}$	**0.12**
5	1.53×10^{-6}	0–30	10	0.046	1.0×10^5	0.12
6	1.53×10^{-6}	0–9	3	0.035	1.0×10^5	0.12
7	1.53×10^{-6}	0–30	10	0.046	1.0×10^5	0.12

carried a Department of Defense (DOD) Space Test Program (STP) experiment to the International Space Station. The STP-H3 experiment included the Canary instrument, a miniature electrostatic analyzer designed by Johns Hopkins University Applied Physics Laboratory and integrated/operated by the United States Air Force Academy (USAFA) Space Physics and Atmospheric Research Center (SPARC). Ground communications are enabled via the National Aeronautics and Space Administration (NASA) Telescience Resource Kit payload interface, permitting operators to command the experiment and download data from a USAFA ground station. Since arriving at the ISS, the SPARC has used Canary to collect ion density versus ion energy sweeps (energy spectrograms) for a wide range of events. One of the first and most dramatic was a fly-around maneuver made by Endeavour on its departure from the ISS on 30 May 2011. A clear ion response was observed corresponding to the NH2 shuttle RCS thruster burn that occurred at 06:39 universal time coordinated at a distance of approximately 5 km from the ISS.

The Canary instrument used in this study is a small electrostatic analyzer configured for the detection of positively charged ions in the energy range (0–1100 eV) [*Feldmesser et al.*, 2010]. When exposed to an incident ion flux, the instrument sensors output the detected total current due to selective ion impact with the sensor surface. Canary is mounted through the ExPA pallet interface on the ISS, which provides electrical power and data handling for the science package. The Canary instrument may be used to characterize surface charging, determine the interaction of spacecraft thruster plumes with the ambient ionosphere, and to identify natural geophysical variability in the ionosphere.

The Canary instrument is composed of seven individual sensors. When the sensor is exposed to an incident ion flux, the ions enter the sensor through the collimator aperture (Figure 1). The aperture cross-section geometry is characterized by width D and length L, such that ions of a divergence angle $\theta_D \leq D/L$ relative to the collimator centerline are transmitted. The transmitted ions enter the electrostatic analyzer (ESA) through the entrance aperture (top energy selector mask) and exit the ESA through the exit aperture (bottom energy selector mask). The top and bottom apertures are positioned diagonally from each other, relative to the ESA centerline (Figure 2). As the ions pass through the ESA, they are deflected through an induced uniform electric field between the parallel plate electrodes comprising the ESA. Ions with the appropriate energy are deflected through the exit aperture and impact the microchannel plate (MCP) below, resulting in amplification of the detected current. The configuration of the apertures, as well as the high aspect ratio (L/D), minimizes sensor contamination due to photons or impact from high-energy charged particles [*Enloe et al.*, 2003].

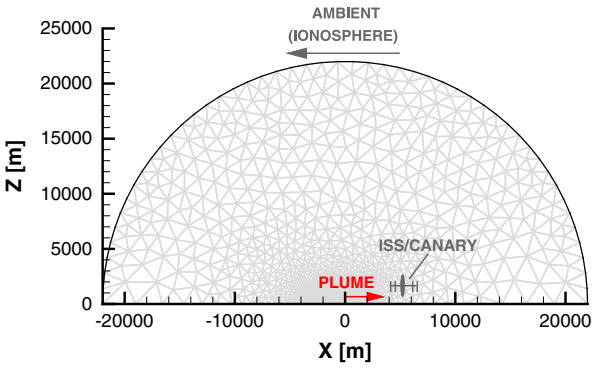

Figure 3. DSMC/PIC computational domain for simulation of STORRM NH2 maneuver. Axis of symmetry lies along x axis and primary jets located at $x = z = 0$ fire in $+x$ direction.

The range of ion energies passing through each electrode pair of the ESA and impacting the respective MCP below results in a piecewise representation of the total current collected over the energy spectrum of the respective sensor. Additionally, a voltage bias is applied across the MCP to amplify low signals via charge multiplication.

The important geometric parameters defining the collimator and ESA, as well as the MCP amplification gain and sensor energy range,

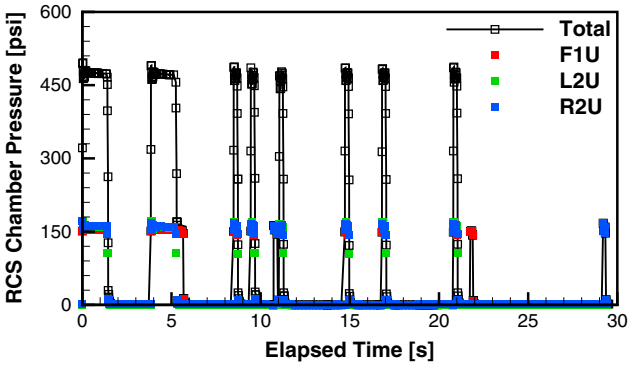

Figure 4. STORRM NH2 RCS chamber pressure output for F1U/L2U/R2U primary jets.

are outlined for each Canary sensor in Table 1. The values reported correspond to the nominal mode of operation of the instrument during the STORRM maneuver. While the Canary sensor is capable of detecting ion energies as high as 1100 eV, this particular configuration (highlighted in bold text in Table 1) targets ion detection over a range of [0–66 eV]. The values outlined are the sensor area A, lower/upper energy limits detected (eV), plate factor P_f, energy resolution $\Delta E/E$, and MCP amplification gain f_{MCP}. The amplification gain is expressed as the elementary charge multiplication for each ion impacting the MCP. These parameters aid in defining the peak energy transmitted through each electrode pair as well as the corresponding energy resolution achieved by each sensor [*Feldmesser et al.*, 2010]. It should be noted that the sensitivity of the ESA instrument is a complex function of many parameters, including the details of the collisional charge exchange processes, the incoming ion plume morphology and ion temperature, local electromagnetic fields, and ISS frame charging in the vicinity of the instrument. In the absence of in situ measurements pertaining to the latter parameters, the following assumptions have been made to facilitate a comparison between the predicted and observed current amplitudes: (1) the ISS frame charging is a typical −20 V, (2) the sensor efficiency factor is based on an ion temperature of 1000 K, (3) the ISS perturbation of the magnetic field is negligible, and (4) the ISS-generated electric field has equipotentials that are parallel to the instrument face. A detailed sensitivity analysis of the total current amplitude in response to variation in these quantities is outside the scope of this work but may be addressed in subsequent studies. The focus of this study involves the comparison of simulation results with output from Canary Sensor 4, which had the largest collection area and yielded the strongest signal during the NH2 maneuver. The remaining sensors 1–3 and 5–7 detected this event as well. The energy and intensity of the detected signatures, however, lie at the very limits of the dynamic range and sensitivity, respectively, of these sensors, making a meaningful comparison difficult.

3. Modeling of Unsteady Plume/Ionosphere Interactions

3.1. Direct Simulation Monte Carlo/Particle-in-Cell Framework

The charge exchange collisions between ambient ions and rocket plume propellant occur under very low density conditions, such that the spacecraft plume density at the nozzle exit is approximately 10 orders of magnitude larger than the ambient ionosphere plasma. The most appropriate numerical method for simulation of these phenomena is the direct simulation Monte Carlo (DSMC) method [*Bird*, 1994]. The plasma formed in this process is subject to self-consistent electrostatic fields, which is most appropriately modeled using the particle-in-cell (PIC) method [*Birdsall and Langdon*, 2004]. The combination of rarefied collisional and plasma phenomena relevant to the physical system of interest is therefore analyzed using the MONACO particle-in-cell (MPIC) simulation tool [*Cai*, 2005], which uses the DSMC and PIC methods simultaneously to model the flow field. The flow conditions and physical models used to simulate the plume interaction with the ambient flow are described below. Details of the MPIC computational framework and physical models that are used in these simulations are outlined in *Stephani and Boyd* [2014].

3.2. Computational Domain and Modeling Approach

The STORRM NH2 burn sequence examined in this study involves thruster firings of three primary jets during a fly-around maneuver of Space Shuttle Endeavour to the ISS. At the initiation of the burn, the shuttle

Table 2. Boundary Conditions for Plume and Ambient Flow Properties

Species	m (kg kmol^{-1})	k_bT/q_o (eV)	V_x (m s^{-1})	n (m^{-3})
Pr	20.7	0.06	2990	$5.8\times10^{23}/1.9\times10^{23}$
O	16.0	0.06	−7640	9.3×10^{13}
O^+	16.0	0.06	−7640	1.0×10^{11}

Table 3. Permitted Interactions Between Plume/Ambient Chemical Species

	Pr	Pr^+	O	O^+
Pr	MEX	MEX/CEX	MEX	MEX/CEX
Pr^+	–	–	MEX	–
O	–	–	MEX	MEX
O^+	–	–	–	–

was located approximately 5 km downstream and 1 km above the orbit of ISS (Figure 3). The primary jets considered in this study are assumed to be coaxial and generate thrust in the $-x$ direction, such that the jets fire toward ISS. The orbital motion of ISS/Endeavour is equivalent to an ionosphere-free stream velocity of 7.6 km/s in the $-x$ direction. The relative orbital motion of ISS/Endeavour is held fixed within the simulation.

The DSMC/PIC simulation is computed on an axisymmetric semicircular domain, with a radius $r = 22$ km and the axis of symmetry along the x axis (Figure 3). The primary jets of Endeavour are positioned at the origin ($x = 0, z = 0$) and are modeled as a combined mass flow from a single nozzle. The nozzle exit plane is an inflow boundary condition with a mass flow determined according to the indicated chamber pressures of the F1U/L2U/R2U thrusters (Figure 4). The thruster burns are characterized as either full burns (in which all three jets are firing), partial burns (one jet is firing), or mixed burns. While the effluent plume and surrounding ionosphere are modeled as collisional, the details of the gas/surface interactions involving the effluent RCS plume and the ISS/Canary instrument are not considered.

The mass flow during these burn periods is the number of thrusters firing multiplied by a nominal mass flow rate $\dot{m} = 1.41$ kg/s per thruster. The burn sequence had a duration of 30 s and is simulated over 0.5 s intervals. The MPIC solution is averaged over the 0.5 s intervals in order to provide an unsteady solution, while reducing the stochastic noise in the macroscopic quantities. The mass flow rate is approximated using the specific impulse of the thrusters, the mass of the orbiter, and a known change in the orbiter velocity resulting from the burn sequence.

3.3. Momentum Exchange/Charge Exchange Collision Dynamics

The chemical system under consideration is composed of four chemical species: spacecraft neutrals/ions and ambient (ionosphere) neutrals/ions. The spacecraft thrusters eject a high-density plume of neutral particles, comprised mostly of water vapor and molecular nitrogen, which expands into the surrounding ambient flow. It is assumed that the spacecraft neutral plume constituents are modeled as a single propellant species with a corresponding ion, referred to as Pr and Pr^+. The molecular weight of the Pr species is equivalent to the molecular weight of the neutral plume mixture, and the collisional properties of Pr and Pr^+ follow those of water vapor. The ambient ionosphere model used in this study is composed of the primary neutral and ion species, O and O^+ found at the ISS orbital altitude of 370 km, following from atmospheric conditions reported in *Kelley* [1989]. Interaction of Pr with the ambient O^+ leads to the formation of Pr^+ through a charge exchange (CEX) reaction. The boundary conditions of the plume at the rocket nozzle exit plane and the ambient flow at the computational domain boundaries are summarized in Table 2. The number density values provided for the propellant species (Pr) at the nozzle exit plane correspond to the full burn (5.8×10^{23} m^{-3}) and the partial burn (1.9×10^{23} m^{-3}) as described above. All velocities reported in Table 2 are in the x direction.

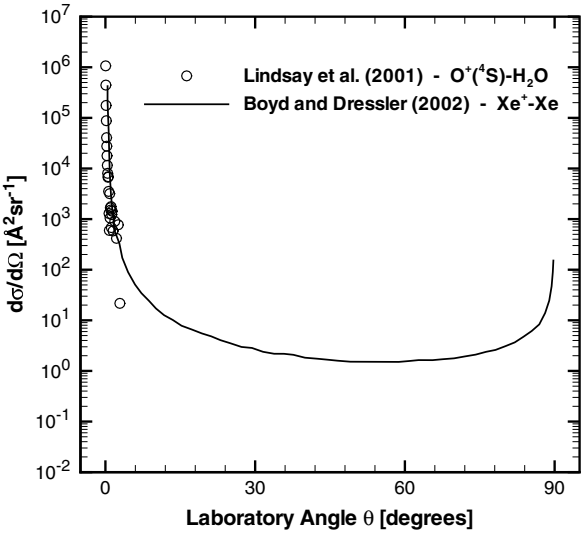

Figure 5. Differential cross sections (DCS) used for modeling charge exchange collision dynamics of O^+–Pr system.

The charge exchange cross sections in this work are adopted from *Dressler et al.* [1996] for reactions between H_2O and O^+. The O^+ ions are allowed to participate in both momentum exchange (MEX) and CEX interactions, but the post collision properties of O^+ are not updated. As will be discussed later in this section, this effectively models the O^+ as being trapped indefinitely on the geomagnetic field lines. The neutral O atoms are allowed to participate in MEX interactions

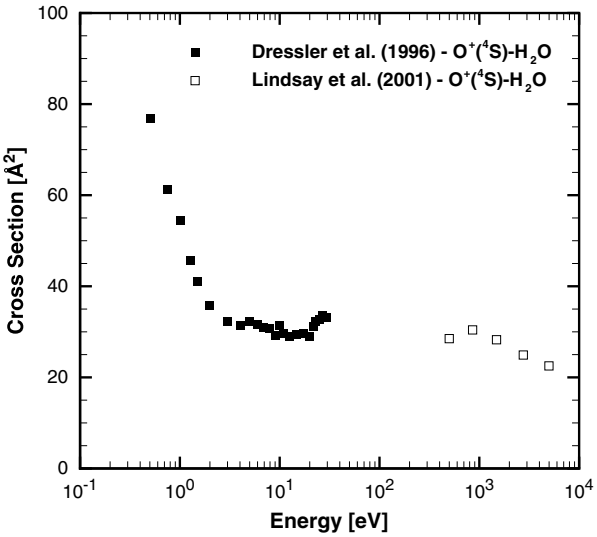

Figure 6. Total cross sections (TCS) used for modeling charge exchange collision dynamics of O^+–Pr system.

only, but the post collision properties are updated. This serves to preserve the ratio of ambient O^+ ions and O neutrals throughout the computational domain. Both Pr and Pr^+ participate in MEX/CEX interactions. A summary of the permitted interactions for this chemical system is provided in Table 3. The rotational and vibrational internal structure of plume constituents (Pr, Pr^+) is neglected in this work.

Heavy particle interactions are treated according to standard DSMC collision dynamics, with the possibility of a charge transfer for neutral/ion collision pairs. The total number of candidate collision partners within a cell is determined using Bird's No-Time-Counter method [*Bird*, 1994]. The probability of a collision event is then determined for these candidate pairs based on the total collision cross section.

Post collision velocities involving neutral/neutral collision pairs are assumed to follow isotropic scattering in the center-of-mass frame of reference, while collisions involving neutral/ion pairs scatter anisotropically, with a strong forward scattering tendency. This anisotropic scattering is incorporated into the MPIC CEX model through the use of experimental differential cross-section (DCS) data. Figure 5 presents measurements of the absolute DCS for CEX scattering of $O^+(^4S)$ with H_2O at 500 eV obtained by *Lindsay et al.* [2001], and by *Boyd and Dressler* [2002]. These measurements were acquired over a limited range of scattering angles, from 0.04 to 2.9° in the laboratory frame of reference. Many of the scattered particles were found to lie within this narrow range, and a comparison of the DCS, integrated from 0 to 3.0°, to an *estimated* total cross section (TCS) indicates that the DCS measurements in Figure 5 capture approximately 74% of the estimated TCS shown in Figure 6.

Although the energies considered in this work ($O(10)$ eV) are significantly lower than those presented in Lindsay et al., this appears to be the only differential cross-section data available for the $O^+ - H_2O$ system, for either ground state $O^+(^4S)$ or metastable $O^+(^2D, ^2P)$. Fortunately, several measurements of the total cross section for the $O^+(^4S) - H_2O$ system are available at lower energy [e.g., *Turner and Rutherford*, 1968; *Dressler et al.*, 1996; *Li et al.*, 1995]. The total cross section for the $O^+(^4S) - H_2O$ system used in this work is thus fitted from measurements by *Dressler et al.* [1996] and *Lindsay et al.* [2001] shown in Figure 6. MEX collisions for Pr – O, O – O and Pr – Pr are modeled using variable hard sphere [*Bird*, 1994] (VHS) total cross sections and isotropic scattering. The corresponding VHS parameters including the reference diameter d_{ref}, reference temperature T_{ref}, and temperature exponent ω are provided in Table 4. Additional details regarding the collision models used in these simulations may be found in *Stephani and Boyd* [2014].

3.4. Magnetic Field Model

In addition to CEX interactions, charged particles in LEO are subject to interaction with Earth's magnetic field. The magnetic field model developed for this work investigates the impact of the geostationary magnetic field on the formation of the spacecraft ion plume, assuming a fixed field line orientation relative to the spacecraft thrust vector.

Immediately after a CEX event, the newly formed ion enters into a gyroscopic orbit about a magnetic field line. This orbit is characterized by the Larmor radius, r_L, and the gyration frequency, ω_L, which are determined according to

Table 4. VHS Parameters for Pr – O, O – O, and Pr – Pr

	d_{ref}	T_{ref}	ω
Pr	4.0Å	273 K	0.75
O	3.0Å	273 K	0.75

$$r_L = \frac{V_{x0}^{Pr^+}}{\omega_L}, \tag{1}$$

$$\omega_L = \frac{q^{Pr^+} B}{m^{Pr^+}}. \tag{2}$$

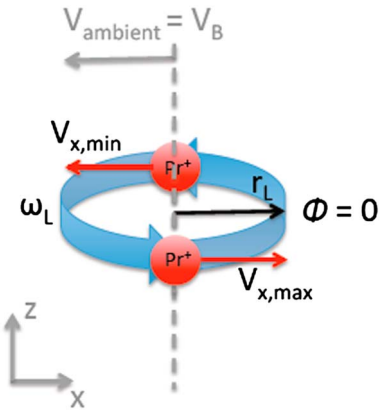

Figure 7. Magnetized Pr^+ ion with gyroscopic motion about magnetic field line.

In equation (1), $V_{x0}^{Pr^+}$ is the initial x velocity of the Pr^+ species entering the gyro-orbit, which is equivalent to the post collision x velocity after a charge exchange reaction. In equation (2), q^{Pr^+} is the fundamental charge, B is the magnetic field strength, and m^{Pr^+} is the molecular mass of the Pr^+ species. From these expressions, it is clear that the magnetic field strength uniquely determines the gyration frequency for a given charged chemical species. The Larmor radius, however, is dependent on both magnetic field strength (through ω_L) as well as on the translational energy of the magnetized ion orthogonal to the field line.

Within the present axisymmetric simulations, the magnetic field lines are assumed to be oriented vertically (parallel to the z axis, shown by dashed lines in Figures 7–9). Thus, only the x velocity component of the magnetized ions follows a gyroscopic motion, while the z velocity component is unimpeded by the magnetic field. Magnetized ions entering a gyroscopic orbit with a nonzero velocity component along the field line thus follow a helical trajectory. The computational frame of reference is held fixed to the spacecraft thruster at the origin, such that the ambient flow, and hence the geomagnetic field lines, has a velocity equivalent to the orbital velocity relative to the spacecraft. The gyroscopic motion due to the magnetic field is imposed on the Pr^+ ions through a time-dependent velocity, which for a constant magnetic field aligned with the z axis, is determined according to

$$V_x^{ion} = V_B \pm \left(V_{x0}^{ion} - V_B\right) sin\left(\frac{q^{ion}B}{m^{ion}}t + \phi^{ion}\right), \tag{3}$$

$$\phi^{ion} = \begin{cases} \pi/2 & \text{if } V_{xo}^{ion} < V_B, \\ 3\pi/2 & \text{if } V_{x0}^{ion} > V_B. \end{cases} \tag{4}$$

The gyroscopic term on the right-hand side is added when $\phi^{ion} = 3\pi/2$ and subtracted when $\phi^{ion} = \pi/2$. The velocity V_{x0}^{ion} is the initial velocity of the magnetized ion as it enters the gyroorbit, which is assumed equal to the post collision velocity of a Pr^+ ion formed through CEX. When the ion enters the orbit, the phase angle, ϕ^{ion}, is specified according to the relative velocity of the ion with respect to the magnetic field line velocity, V_B. This is shown schematically in Figure 7, for a case in which the ambient flow (and therefore the field line velocity) is directed to the left. If the ion has a velocity to the left relative to the field line, the ion enters the orbit with a phase of $\phi^{ion} = \pi/2$. This represents a minimum orbital velocity, and the ion velocity is thus $V_{x0} = V_{x,min}$. If the ion has a velocity to the right relative to the field line, the ion enters the orbit with a phase of $\phi^{ion} = 3\pi/2$, and the ion velocity corresponds to $V_{x0} = V_{x,max}$. The time t in equation (3) is initialized to zero when the ion enters the orbit and is advanced by the simulation time step. The gyration frequency in equation (2) is constant and has a value $\omega_L = 233$ rev/s for the $B = 0.5$ Gs cases. The time step used in the simulations is $dt = 2.5 \times 10^{-4}$ s, which is on the order of the mean collision time for binary particle collisions. Thus, a single gyroscopic orbit is resolved by approximately 17 simulation time steps.

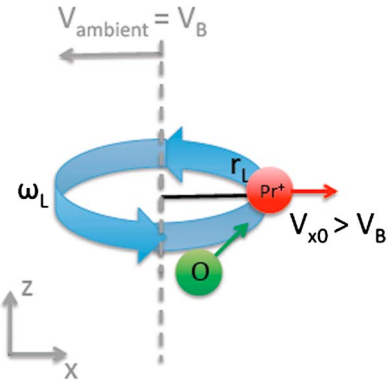

Figure 8. Magnetized Pr^+ ion undergoes MEX collision with either O or Pr. Post collision velocity of Pr^+ is used to update the phase angle.

It is important to note that while the plume gas dynamics are modeled as an axisymmetric solution, the magnetic field model only modifies the gyroscopic motion of the Pr^+ ions in the x direction. Consideration of the gyroscopic motion in the y direction would require a full three-dimensional simulation, as this component cannot be modeled in a physically consistent way

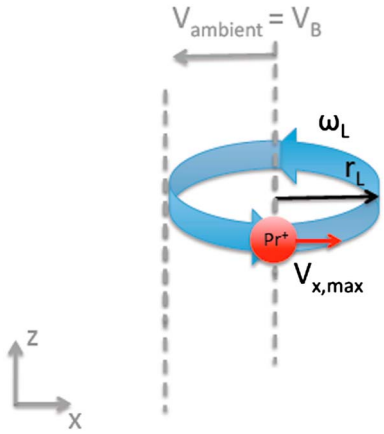

Figure 9. Updated phase angle defines new guiding center, providing a mechanism for cross-field diffusion within the magnetic field model.

within the axisymmetric simulation. This allows for a quasi-axisymmetric solution in which the two-dimensional (x/z) gyroscopic motion is imposed on the axisymmetric solution of the plume and ambient flows.

Once magnetized, the motion of the Pr^+ ions is a superposition of the magnetic field velocity and the unsteady gyration velocity in the x direction. In a collisional flow, however, these magnetized ions may undergo collisions with other particles. A collision resulting in both momentum and charge exchange would effectively "demagnetize" the Pr^+ ion, and the resulting Pr neutral would follow a linear trajectory according to its post collision velocity. This demagnetization process is modeled for Pr^+–Pr charge transfer only, as described in section 3.3 and summarized in Table 3.

It is also possible for a collision between a magnetized Pr^+ ion and a neutral particle to result in momentum exchange only. Although the Pr^+ ion keeps its charge and remains magnetized, the momentum exchange will effectively transfer the Pr^+ onto a new orbit with a new guiding center. This process is shown schematically in Figures 8 and 9, in which a magnetized Pr^+ ion undergoes a MEX collision with an O atom. In this particular scenario, the Pr^+ ion velocity has a phase $\phi^{ion} = 0$ and thus has zero velocity relative to the field line guiding center. Upon collision, the momentum transfer will result in a finite post collision x velocity component (e.g., to the right as shown by the red arrow). This post collision velocity defines the initial velocity V_{x0}^{ion} for a different orbit about a new guiding center, shown in Figure 9. To define the guiding center of the new orbit, the phase angle ϕ^{ion} must be evaluated after each MEX collision using the velocity criteria specified in equation (4), where V_{x0}^{ion} is taken as the Pr^+ post collision velocity.

This treatment of MEX collisions involving magnetized Pr^+ ions provides a mechanism for cross-field diffusion of the spacecraft ions within these simulations. The cross-field diffusion process is modeled for both Pr^+–Pr and Pr^+–O momentum exchange events, as summarized in Table 3. As mentioned in section 3.3, the ambient O^+ ions are modeled as being trapped indefinitely on the magnetic field lines to preserve the ambient conditions. In consideration of the gyroscopic parameters in equations (1) and (2), the O^+ ions are modeled as magnetized on field lines of infinite strength, $B \rightarrow \infty$. An investigation of the impact of the magnetic field strength on the development of both the spacecraft neutral and ion plumes is presented in *Stephani and Boyd* [2014].

4. Results

In this section, unsteady results are presented from the simulations of the STORRM NH2 burn sequence. The flow field solutions are presented first, to provide a qualitative overview of the ion plume development during the early parts of the NH2 burn sequence. The simulation results are then analyzed using a "simulated" sensor, and results from the analysis are compared to the total current observed by Canary from ISS.

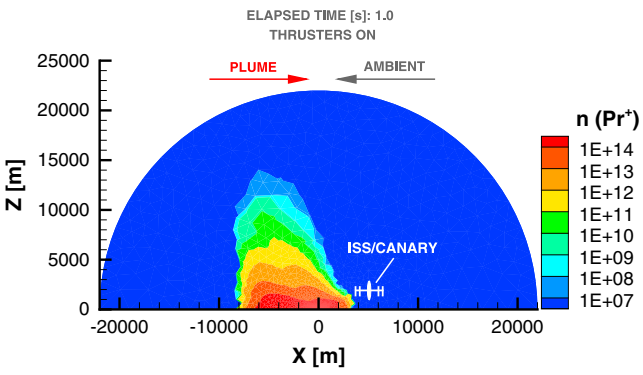

Figure 10. Contours of Pr^+ number density (m^{-3}), 1.0 s after initiation of the NH2 burn sequence.

4.1. Unsteady Flow Field Results: $t = 1.0$ s, 2.0 s, 3.7 s, 5.7 s

The unsteady flow field results are presented in Figures 10–13 during the early portion of the NH2 burn sequence. The thrusters begin firing at $t = 0$ s, generating a neutral plume with initial velocity in the $+x$ direction. The neutral particles undergo charge

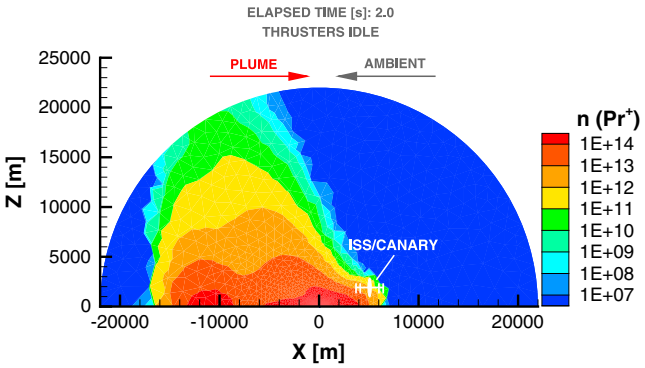

Figure 11. Contours of Pr^+ number density (m^{-3}), 2.0 s after initiation of the NH2 burn sequence. Note that the ion plume reaches Canary after 2.0 s delay.

exchange with the ambient ions, and the number density contours in Figures 10–13 show the development of the resulting propellant ion plume.

Figure 10 shows the Pr^+ ion plume 1.0 s into the burn sequence. The contour levels are distributed exponentially to highlight the difference in concentration of the plume in the far field. The contours are saturated at a number density of 1×10^7 m^{-3}, which corresponds to a current density that is well below the lower threshold (1×10^{12} m^{-3}) for detection by the Canary sensor. The majority of neutral Pr particles initially move in the $+x$ direction with the thruster exit velocity. After charge exchange ionization, however, the Pr^+ ions become magnetized and gyrate about the geostationary magnetic field lines, which in this frame of reference, move with the ambient flow in the $-x$ direction. Although the ion plume does propagate in the $+x$ direction, the highest plume concentration is found downstream of the thruster origin.

It is important to keep in mind that the Pr neutral particles are not impeded by the magnetic field lines and, with the exception of binary collisions, are free to propagate upstream against the rarefied ambient free stream. This provides a strong concentration of Pr upstream of the thruster, which in turn may undergo charge exchange and contribute to the Pr^+ concentration upstream of the thruster. These ions may form either upstream or downstream of the thruster but are constantly swept downstream by the magnetic field lines. All thrusters are active at this point, but the plume has not yet reached the Canary sensor, which is shown 5 km upstream and 1 km above the thruster axis of symmetry.

Figure 11 shows the Pr^+ ion plume 2.0 s into the burn sequence. At this point, the thrusters are idle, but the ion plume generated from the first burn has now reached the Canary sensor. This delay corresponds to the time of flight for the Pr neutral plume to reach the location of the Canary sensor and, as will be seen in the next section, is also observed in the Canary data. The plume continues to propagate downstream of the thruster, but it is also observed that the ion plume expands outward in the z direction. Recall that the motion of gyrating ions along the field lines is unimpeded, allowing the ion plume to spread outward.

After 3.7 s, the thrusters are again idle, and the ion plume has propagated more than 10 km upstream of the thruster origin (Figure 12). The ion plume persists more than 20 km downstream of the thruster, although the concentration does drop off slightly before the end of the domain. The thrusters are again turned on, and the ion plume concentration increases near the thruster after 5.7 s, as shown in Figure 13.

In Figures 11–13, it is apparent that the ion plume remains in high concentration near the Canary sensor, with Pr^+ number densities greater than 1×10^{12} m^{-3}. This is the case with thrusters on and idle, which suggests that the concentration of neutral Pr particles upstream of the thruster from earlier thruster firings undergo charge exchange reactions and work to replenish the ion plume. Although the concentration of Pr^+ ions remains high in the vicinity of the Canary instrument, it is important to note that not all of the Pr^+ ions present will be detected by the Canary sensor. Further analysis is therefore required to determine the total current predicted by the simulation for comparison to the observation data.

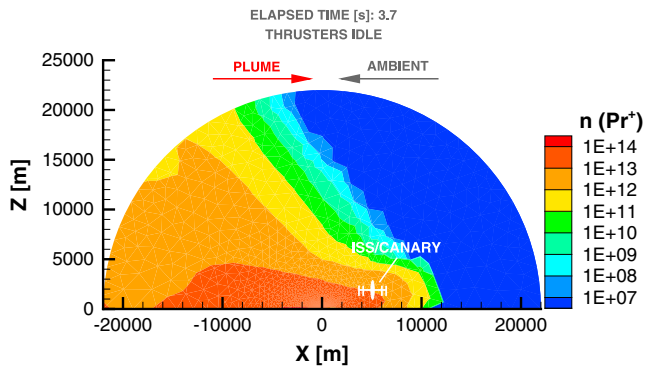

Figure 12. Contours of Pr^+ number density (m^{-3}), 3.7 s after initiation of the NH2 burn sequence.

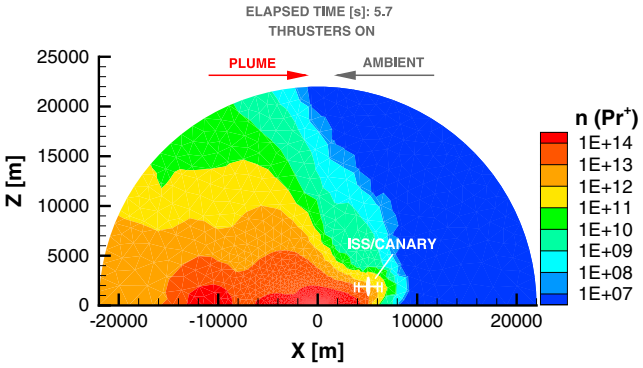

Figure 13. Contours of Pr^+ number density (m^{-3}), 5.7 s after initiation of the NH2 burn sequence.

4.2. Comparison Between Canary and Simulated Plume Data

The unsteady flow field results generated by MPIC provide a detailed picture of the development of the Pr^+ plume. The results above allow for a quantification of the simulated *total* charge density at the location of the Canary sensor throughout the burn sequence. However, as discussed earlier in section 2, the sensor provides a piecewise representation of the total current at the sensor location. Furthermore, the collimator geometry restricts the transmission of ions through the sensor to those ion trajectories within a specified divergence. Therefore, a number of considerations must be made in the analysis of the simulation data to provide a consistent comparison between the predicted and measured current values.

To facilitate this comparison, a "simulated sensor" is employed to determine the equivalent current that would be detected after transmission through the collimator, ESA and MCP regions of the sensor. Within the simulation, the ion energy distribution function (IEDF) is sampled for all Pr^+ ions which would impact the Canary sensor surface within the specified divergence angle relative to the sensor surface normal. This is equivalent to sampling the IEDF for all Pr^+ ions which cross a prescribed sampling surface in the positive radial direction from the thruster origin, within the specified divergence angle.

The sampled energy distribution is numerically integrated piecewise over the energy spectrum, based on the collective range of ion energies passing through each electrode pair of the ESA of Canary Sensor 4. As outlined in Table 1, Sensor 4 is configured to detect ions at 30 voltage sweep points, evenly spaced over a range of 0–66 eV, with a resolution specified by the ratio $\Delta E/E$ at each sweep voltage. Based on the configuration of the Canary sensor during the NH2 burn, the piecewise integration of Sensor 4 is evaluated over each energy increment expressed as

$$\delta E_i^{\pm} = E_i\,(1 \pm \Delta E/2E) \tag{5}$$

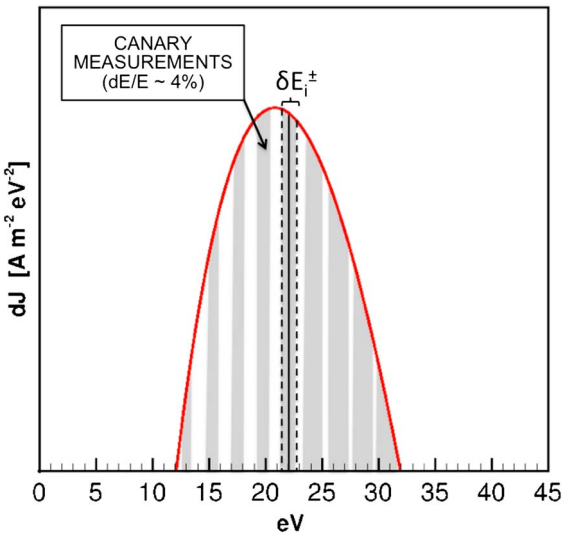

Figure 14. Schematic of piecewise integration used in simulated sensor analysis, representative of total current measured by Canary.

$$E_i = 2.2i\ (\text{eV}),\ i \in [1, 30] \tag{6}$$

Note that this energy increment increases linearly with energy, resulting in a piecewise integration represented schematically in Figure 14. In addition to the piecewise integration, the current determined from the simulated sensor analysis is also adjusted to account for the ion transmission efficiency through the ESA, f_{ESA}, the MCP amplification gain, f_{MCP}, the instrument noise floor, f_{floor}, and the sensor surface area, A. The instrument noise floor is determined from measurements made for the null condition, in which the null data is acquired by the sensor in the absence of spacecraft thruster activity. This noise floor was determined as $f_{floor} = 3.2 \times 10^{-9}$ A, which is equivalent to a noise floor of 9.6×10^{-8} A when summed over the 30 voltage sweep

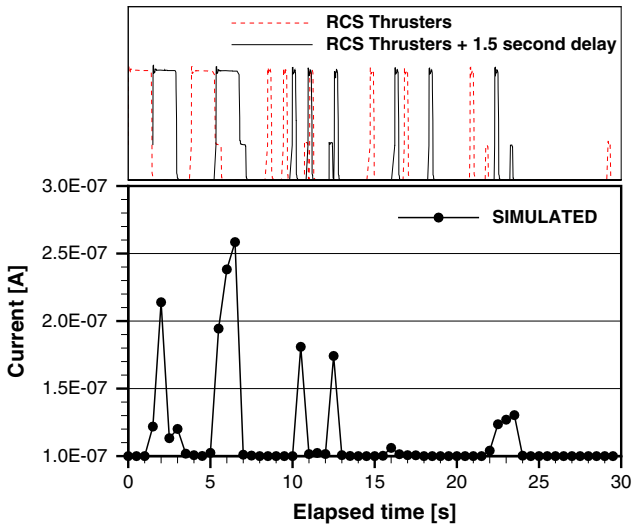

Figure 15. Predicted total current as a function of time during the STORRM NH2 maneuver, as determined by the simulated sensor analysis. Current is plotted on a linear scale, and null data are shown as values of 9.6×10^{-8} A. RCS thruster chamber pressure (original and shifted) as a function of time is shown above.

points of the Canary instrument. Thus, the predicted total current detected by Sensor 4 is expressed as

$$I_{\mathrm{MPIC}} = J_{\mathrm{MPIC}} \sum_{i=1}^{30} \left(\int_{0\ \mathrm{eV}}^{66\ \mathrm{eV}} f(E)\mathrm{d}E \right) f_{\mathrm{MCP}}\, f_{\mathrm{ESA}}\, f_{\mathrm{floor}}\, A. \quad (7)$$

In equation (7), J_{MPIC} is the current density at the location of the sensor and $f(E)$ is the ion energy distribution function (described above). The results from the simulated sensor analysis are plotted in Figure 15, which shows the total current as a function of time over the duration of the NH2 burn sequence. Results are plotted on a linear scale, and values are reported at a sampling frequency of 2.0 Hz (null values are suppressed as values of 9.6×10^{-8} A). The corresponding chamber pressure of the F1U/L2U/R2U RCS jets are shown as a function of time in the top figure (repeated from Figure 4) to aid in discussion.

The beginning of the NH2 burn sequence is at time $t = 0$ s, indicated by the increase in the total RCS thruster chamber pressure shown by the dashed red line. The ion plume is not detected by the simulated sensor until approximately 1.5 s after the start of the burn sequence. Recalling the discussion of the flow field data presented in section 4.1, this is consistent with the predicted propagation time for the ion plume to reach the Canary sensor. The first ion plume detection in the simulated total current occurs at $t = 1.5$ s, at which time the thrusters are idle as shown by the dashed red line. However, if the RCS thruster chamber pressure curve is shifted by the 1.5 s delay (shown by the solid black line), it is observed that the first ion plume detection in the simulation data corresponds precisely to the initial firing of the F1U/L2U/R2U jets. The first peak in the simulated total current occurs at $t = 2.0$ s, in the middle of the first thruster firing as indicated by the black line on the RCS thrusters plot.

The second peak in the simulated total current data occurs in correspondence with the second thruster firing (again, including the 1.5 s delay). This trend continues throughout the NH2 burn sequence, although at later times, the thrusters are turned on for very short bursts of approximately 0.5 s. In comparison, the first two thruster burns included all three jets and lasted for approximately 1.5–2.0 s. These shorter thruster burns in the later portion ($t > 15$ s) generate total current signals that are slightly weaker than the first two detected current signals: the total current detected at 2.0 s and 6.5 s are 2.1×10^{-7} A and 2.6×10^{-7} A, respectively, while the total current detected at 16.0 s and 23.0 s are 1.1×10^{-7} A and 1.3×10^{-7} A.

A comparison of the simulated total current and the total current measured by Canary is presented in Figure 16. The simulated total current is repeated from Figure 15 and is compared against the Canary data using a linear scale to highlight the comparison of peaks in the signal. The peaks in the detected current are qualitatively similar between the Canary measurements and simulated data. Again, the peaks in the simulated current coincide with the chamber pressure output and remain relatively distinct; however, the Canary data show that the peaks in signal become more ambiguous at later times when the thruster burns are short in duration. It should be noted that the Canary data were collected at a sampling rate of 1 Hz, and it is possible that a higher sampling rate would have captured the short burst of current that characterize the later thruster firings.

From a quantitative perspective, the simulated total current signal compares very well to the total current measured by Canary, particularly when the thruster burn was long in duration or closely spaced in time.

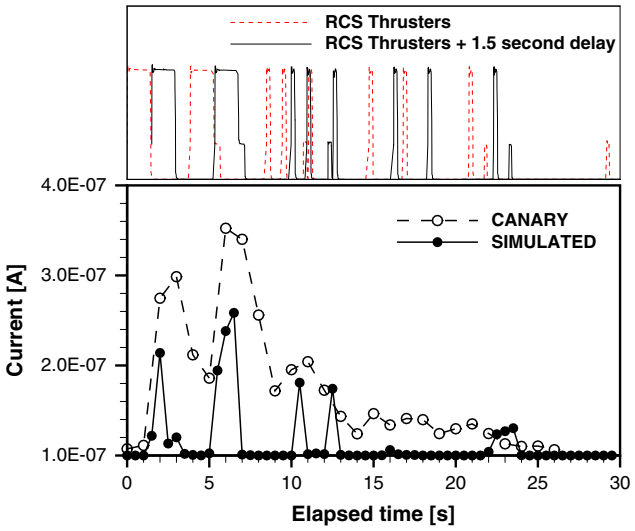

Figure 16. Comparison of Canary and simulated total current as a function of time during the STORRM NH2 maneuver. RCS thruster chamber pressure (original and shifted) as a function of time is shown above.

The peak total current predicted by the simulation data occurred simultaneously (within the sampling frequency) with the peak Canary signal, at $t = 6.0$ s. The simulation data predicted a peak total current of 2.6×10^{-7} A, while the Canary sensor measured a peak total current of 3.5×10^{-7} A, which is a factor of 1.4 higher than the predicted simulation value, as seen in Figure 16. In periods of the NH2 maneuver where the signal was considerably weaker (e.g., $t > 15$ s), the total current measured by Canary remained slightly above 1.0×10^{-7} A, while the predicted total current from the simulation analysis remained at or near the noise floor, as shown in Figure 16.

5. Summary and Conclusions

The primary focus of this work was to examine the interaction between Space Shuttle Endeavour's RCS plumes and the ambient ionosphere during the STORRM NH2 maneuver. During this event, RCS jets were fired during a fly-around maneuver, and the neutral plume emitted during the thruster burns formed a relatively high density ion plume through charge exchange (CEX) reactions with the ambient ionosphere flow in low-Earth orbit (LEO). This ion plume signal was measured as a detected current by the Canary instrument on ISS. To provide a more detailed picture of the plume/ionosphere interaction, a model based on a combined DSMC/PIC methodology was used to simulate the STORRM NH2 maneuver. The DSMC/PIC model properly captured the nonequilibrium collisional and plasma phenomena that are relevant in the rarefied plasma environment in LEO. Also of great interest was the influence of the geomagnetic field on the ion plume.

The unsteady simulation results were generated for the entire duration of the STORRM NH2 maneuver based on the real-time RCS chamber pressure data provided by NASA. After a 1.5 s time-of-flight delay, the ion plume was observed to reach the location of the Canary sensor. The highest ion plume concentration was found downstream of the thruster origin, as the ions formed through charge exchange reactions are immediately trapped in gyroscopic motion about the geostationary magnetic field lines. In the frame of reference fixed to the thrusters, the magnetic field lines move downstream of the thrusters at a velocity equivalent to the orbital velocity of the spacecraft.

The predicted total current from the simulated sensor analysis showed good qualitative agreement to the RCS chamber pressure data, with the inclusion of the 1.5 s time-of-flight delay. The peaks in the predicted total current corresponded precisely with the thruster burn sequence, although the strength of the signal was found to diminish at later times as the thruster burns became short in duration and more intermittent. Finally, the comparison of the simulated total current to the Canary measurements showed very good agreement, both qualitatively and quantitatively. The peak total current from the simulation analysis was within a factor of 1.4 (underpredicted) of the Canary detected current.

Acknowledgments

We gratefully acknowledge the support of Air Force Research Laboratory (AFRL) Space Vehicles Directorate and Barron Associates, Inc. Work was performed under subcontract to Barron Associates, Inc. through AFRL contract FA9453-11-C-0181. Space Shuttle thruster data used in this research were provided by NASA and the DOD Space Test Program. The authors also wish to acknowledge contributions made to this work by J. FitzGerald, K. Kalamaroff, D. Musick, and P.C. Neal. The STP-H3 payload complement is integrated and flown on the ISS under the management and direction of the Department of Defense Space Test Program, Human Spaceflight Payloads Office. Information regarding the observation data used to produce the results of this paper may be obtained from M. G. McHarg (Matthew.Mcharg@usafa.edu). Computational resources and technical support were provided by the Center for Advanced Computing at the University of Michigan.

Larry Kepko thanks the reviewers for their assistance in evaluating this paper.

References

Bernhardt, P., et al. (2012), Ground and space-based measurement of rocket engine burns in the ionosphere, *IEEE Trans. Plasma Sci.*, *40*(5), 1267–1286.

Bird, G. (1994), *Molecular Gas Dynamics and the Direct Simulation of Gas Flows*, Oxford Univ. Press, Oxford, U. K.

Birdsall, C., and A. Langdon (2004), *Plasma Physics via Computer Simulation*, Taylor and Francis, New York.

Boyd, I., and R. Dressler (2002), Far field modeling of the plasma plume of a Hall thruster, *J. Appl. Phys.*, *92*(4), 1764–1774.

Burke, W., L. Gentile, J. Machuzak, D. Hardy, and D. Hunton (1995), Energy distributions of thruster pickup ions detected by the Shuttle Potential and Return Electron Experiments during TSS 1, *J. Geophys. Res.*, *100*(A10), 19,773–19,790, doi:10.1029/95JA01214.

Cai, C. (2005), Theoretical and numerical studies of plume flows in vacuum chambers, PhD dissertation, Univ. of Michigan, Ann Arbor, Mich.

Dahl, D., and J. Delmore (1987), *The SIMION PCI/PS2 User's Manual Version 3.1*, Idaho National Engineering Laboratory, Idaho Falls.

Drakes, J., and D. Swann (1999), DSMC computations of the Progress-M spacecraft retrofiring exhaust plume, paper presented at AIAA Aerospace Sciences Meeting (37th) and Exhibit, Paper No. AIAA-99-0975, Ft. Belvoir Defense Technical Information Center, Reno, Nev. on January 11-14, 1999.

Dressler, R., M. Bastian, D. Levandier, and E. Murad (1996), Empirical model of the state-to-state dynamics in near-resonant hyperthermal X+ + H2O charge-transfer reactions, *Int. J. Mass Spectrom. Ion Processes*, *159*, 245–256.

Enloe, C., K. Habush, R. Haaland, T. Patterson, C. Richardson, C. Lazidis, and R. Whiting (2003), Miniaturized electrostatic analyzer manufactured using photolithographic etching, *Rev. Sci. Instrum.*, *74*(3), 1192–1195.

Feldmesser, H., M. Darrin, R. Osiander, L. Paxton, A. Rogers, J. Marks, M. McHarg, R. Balthazor, L. Krause, and J. FitzGerald (2010), Canary: Ion spectroscopy for ionospheric sensing, paper presented at SPIE 7691, Space Missions and Technologies, Orlando, Fla., doi:10.1117/12.850414.

Kaplan, C., and P. Bernhardt (2010), Effect of an altitude-dependent background atmosphere on shuttle plumes, *J. Spacecr. Rockets*, *47*(4), 700–704.

Karabadzhak, G., Y. Plastinin, B. Khmelinin, V. Teslenko, N. Shvets, J. Drakes, D. Swann, and W. McGregor (1997), Experimentation using the Mir station as a space laboratory, paper presented at AIAA Aerospace Sciences Meeting, Reno, Nev., AIAA Paper No. AIAA-97-0288.

Kelley, M. C. (1989), *The Earth's Ionosphere*, Acad. Press, San Diego, Calif.

Li, X., Y.-L. Huang, G. Flesch, and C. Ng (1995), Absolute total cross sections for the ion-molecule reaction $O^+(^4S^o)+H_2O$, *J. Chem. Phys.*, *102*(5100–5101).

Lindsay, B., R. Rejoub, D. Sieglaff, and R. Stebbings (2001), Charge transfer of keV O^+ ions with CO and H_2O, *J. Phys. B: At., Mol. Opt. Phys.*, *34*, 2159, doi:10.1088/0953-4075/34/11/308.

McMahon, W., R. Salter, R. Hills, and D. Delorey (1983), Measured electron contribution to shuttle plasma environment, paper presented at Shuttle Environment and Operations Meeting, AIAA Paper No. AIAA-83-2598, Washington, D. C.

Stephani, K., and I. Boyd (2014), Detailed modeling and analysis of spacecraft plume/ionosphere interactions in low Earth orbit, *J. Geophys. Res. Space Physics*, *119*, 2101–2116, doi:10.1002/2013JA019222.

Stuit, T. (2011), Designing the STS-134 re-rendezvous: A preparation for future crewed rendezvous missions, paper presented at AIAA SPACE 2011 Conference Exposition Online Proceedings, AIAA Paper No. 2011-7189, Timothy Stuit United Space Alliance, Houston, Tex.

Turner, B., and J. Rutherford (1968), Charge transfer and ion-atom interchange reactions of water vapor ions, *J. Geophys. Res.*, *73*, 6751–6758.